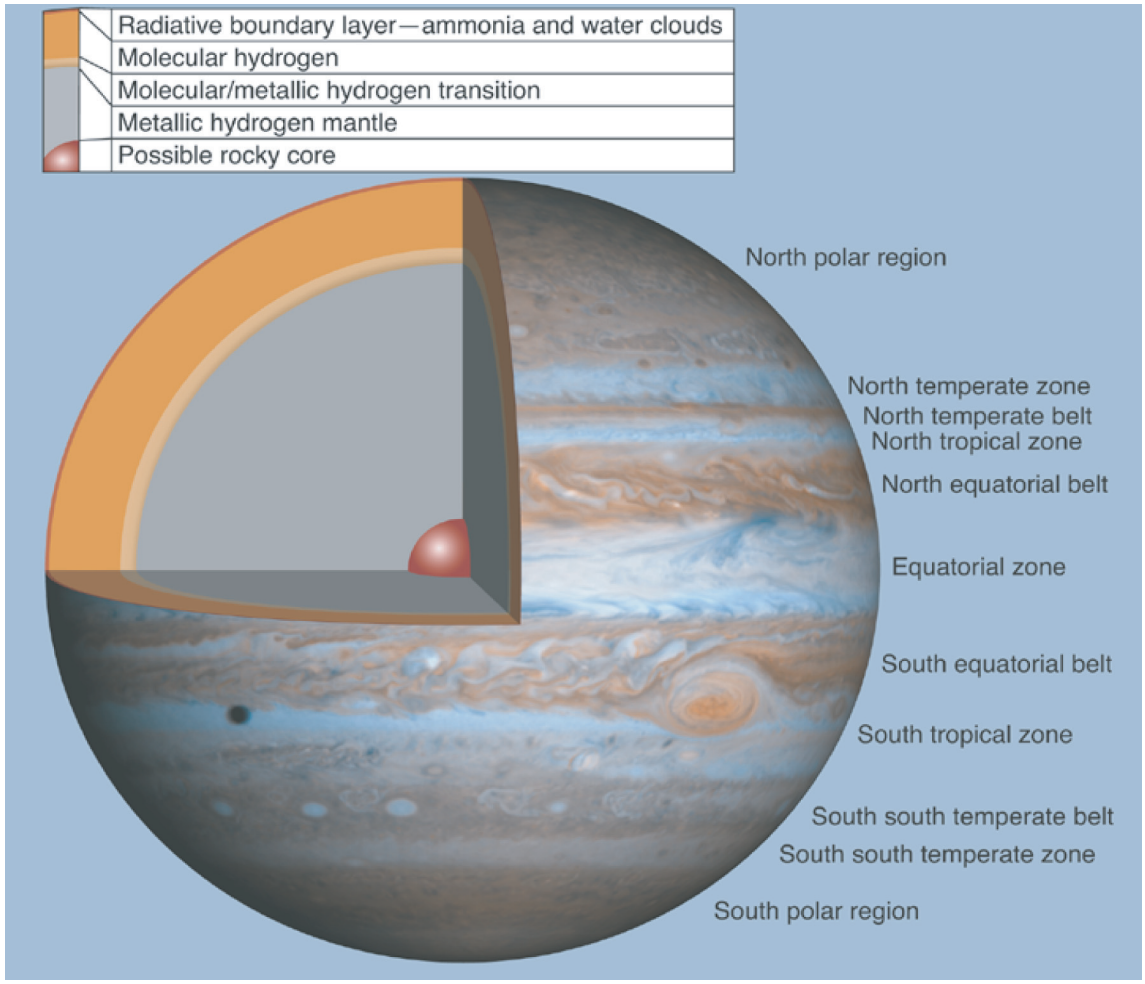

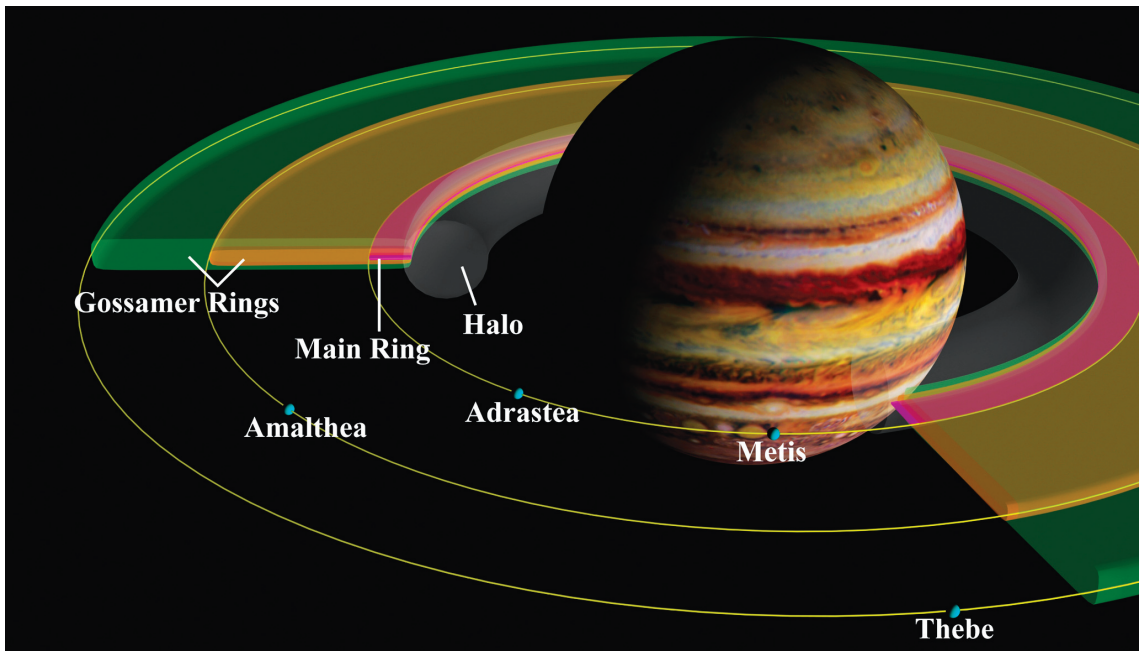

Plate 1, (a) Figure 1.3: Cut-away view of Jupiter showing the internal structure (see Chapter 3). The cloud bands are labeled on an image of Jupiter taken by *Cassini* in November 2000.

(b) Figure 11.1: A cut-away view of the components of Jupiter's ring system is shown in relation to Jupiter and to the small ring-moons that are described in this chapter. The innermost and thickest ring, shown as a torus, is the *halo* whose outer edge ends at the narrow and flat *main ring*. The main ring is circumscribed by the satellite Adrastea's orbit; it may be partly composed of fine particles knocked off Adrastea, and a somewhat larger moon Metis located about 1000 km closer to the planet. Thebe and Amalthea, satellites that are larger still, supply dust that forms the thicker, washer-like *gossamer rings*; the thicknesses of the gossamer rings are determined by the inclinations of these two satellite orbits. A very faint extension (not shown) of the outer gossamer ring reaches beyond Thebe's orbit. From Ockart-Bell *et al.* (1999).

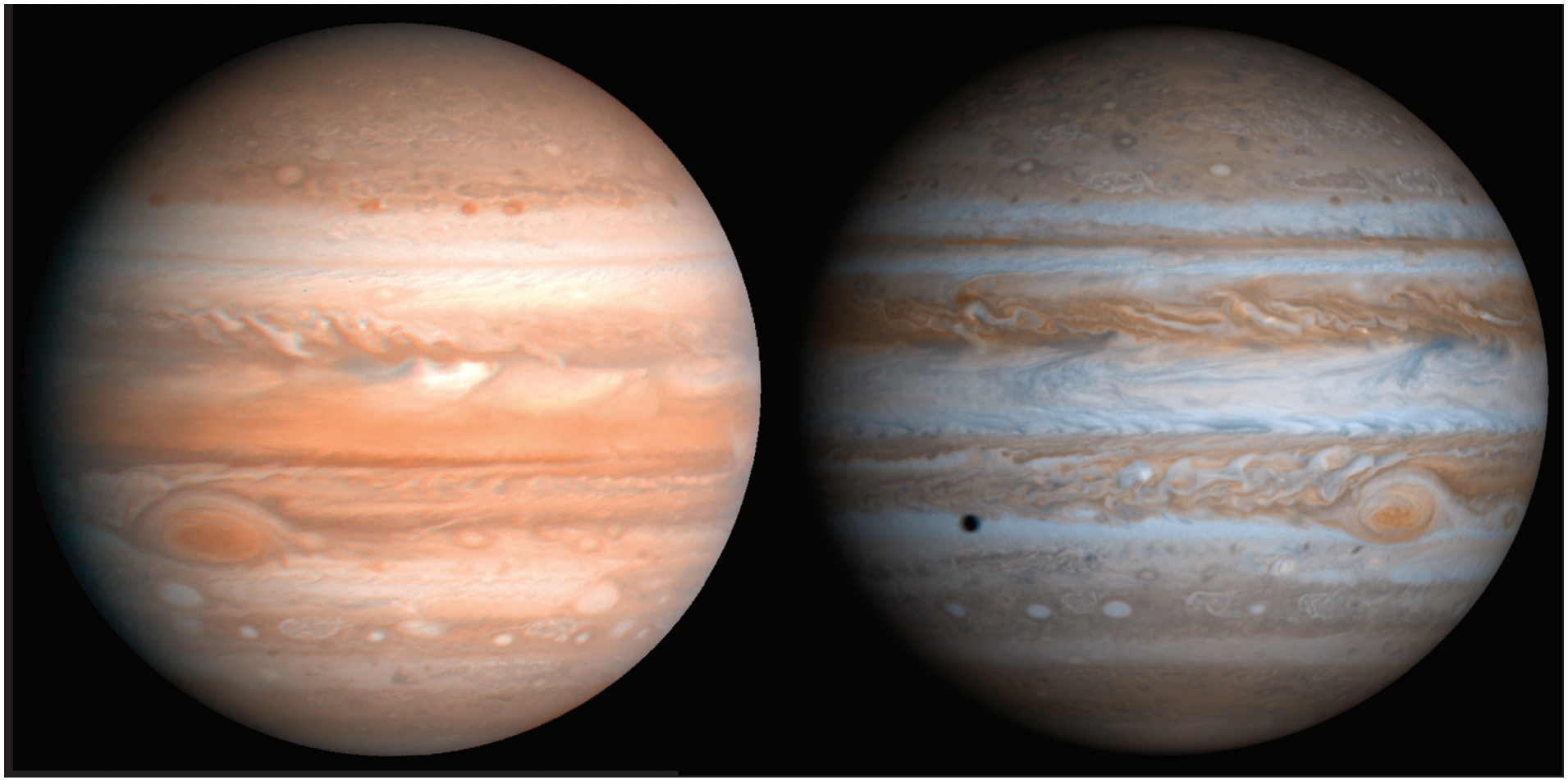

Plate 2, Figure 6.1: Whole disk views of Jupiter. The left image is from *Voyager 2* in June 1979. The right image is from *Cassini* in November 2000.

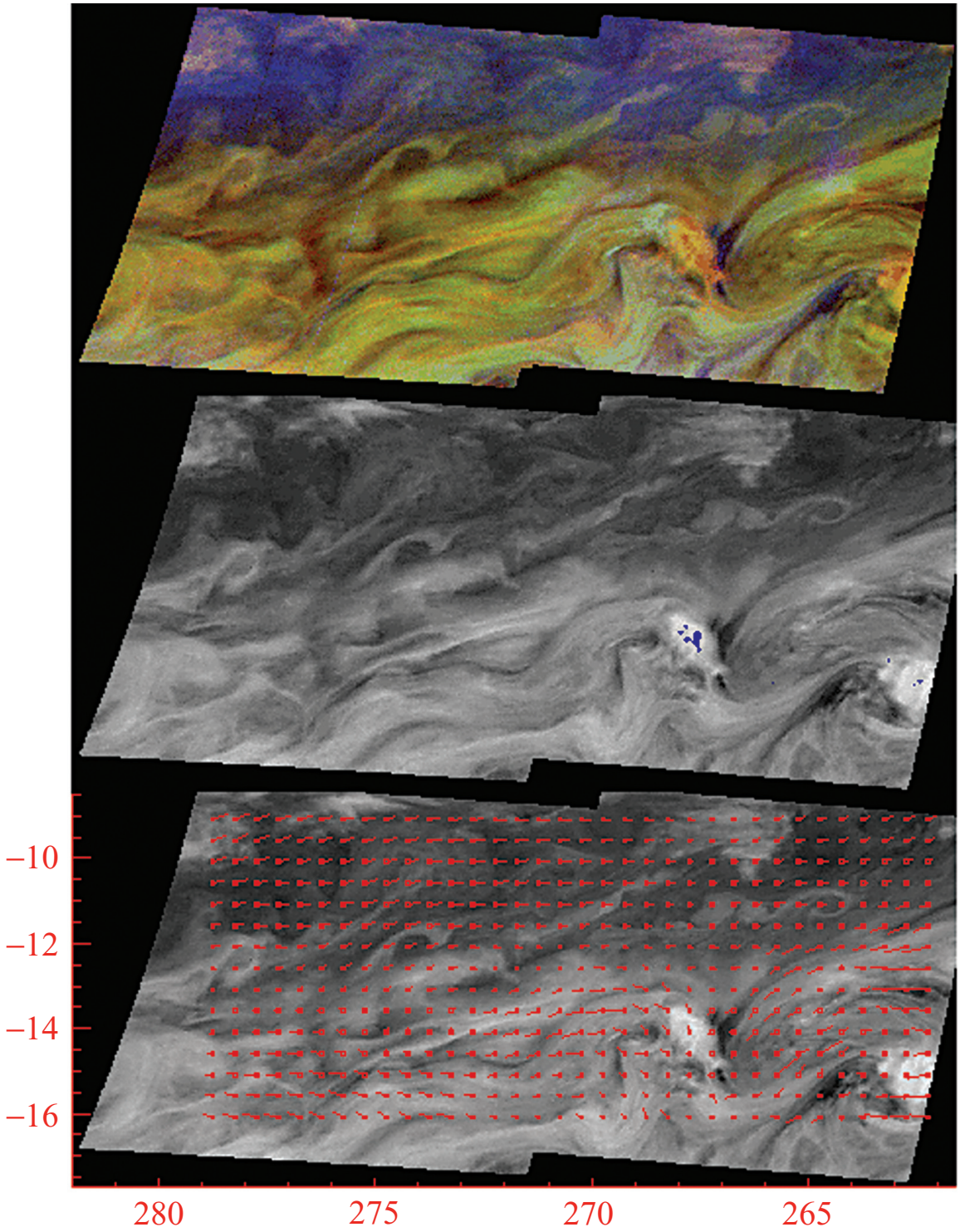

Plate 3, Figure 6.17: Lightning storms (Gierasch *et al.* 2000) in the southern hemisphere. The top panel is a superposition of a continuum wavelength (756 nm) in the red plane, a medium methane band (727 nm) in the green plane, and a strong methane band (889 nm) in the blue plane. The location of lightning is shown by the blue overlay on to a continuum image in the middle panel. Note the close proximity of red (deep) features and bright white (high) features to the flash locations. The bottom panel shows velocity vectors derived from three time-steps in the continuum. The flags point downwind, and the largest flag corresponds to a speed of 70 m s^{-1}. The large-scale flow structure is eastward near the top of the frame (the north edge) and westward near the bottom. In the southern hemisphere this represents cyclonic shear. Approximate latitude and longitude are indicated on the bottom panel. This region is $\sim 30^{\circ}$ west of the Great Red Spot.

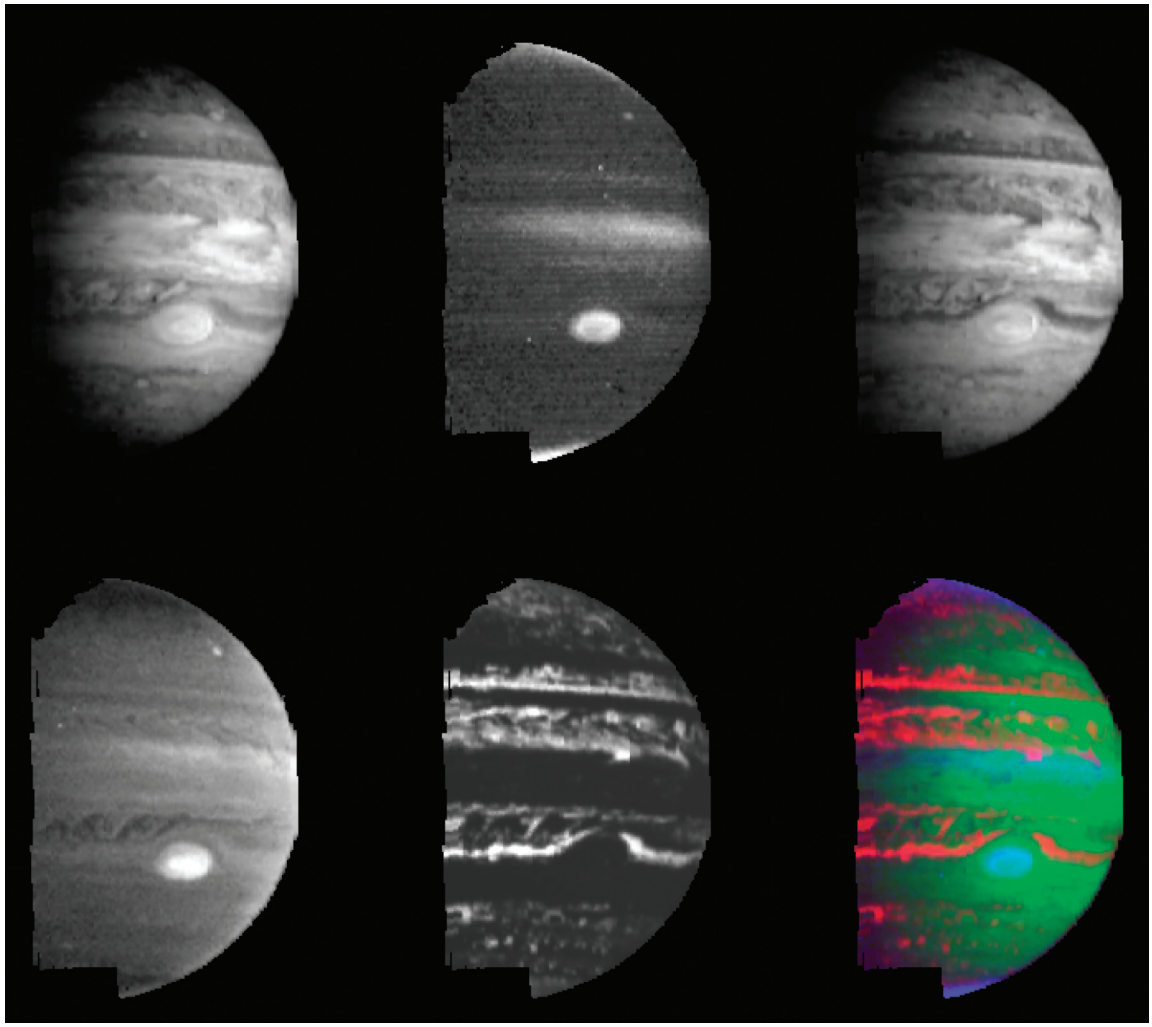

Plate 4, Figure 5.5: These images of Jupiter at various near-infrared wavelengths were taken by the Near-Infrared Mapping Spectrometer (NIMS) during the second orbit (G2) of the *Galileo* spacecraft on September 5, 1996. The differences are due primarily to variations in the altitudes and opacities of the cloud systems. The top left and right images, taken at 1.61 μm and 2.73 μm respectively, are in spectral regions of low molecular absorption giving relatively clear views of the deep atmosphere, down to approximately the 3 bar level. The top center image, at 2.17 μm, shows only the highest altitude clouds and hazes, due to strong absorption by hydrogen. The Great Red Spot, the highest equatorial clouds, a small feature at mid-northern latitudes, and thin, high photochemical polar hazes can be seen. In the lower left image, at 3.01 μm, deeper clouds can be seen, but extreme depths are obscured by gaseous ammonia and methane absorption. In the lower middle image, at 4.99 μm, the planet is seen in thermal emission from the deep, warm atmosphere. The false color image (lower right) is a composite in which red areas denote high temperature emission from the deep atmosphere in areas of minimal cloud cover; green denotes cool tropospheric clouds; blue denotes the cold upper troposphere and lower stratosphere. The purplish, yellowish and light blue regions are those with high concentrations of small-particle hazes with various scattering and absorption properties, including high-level hazes of photochemical origin.

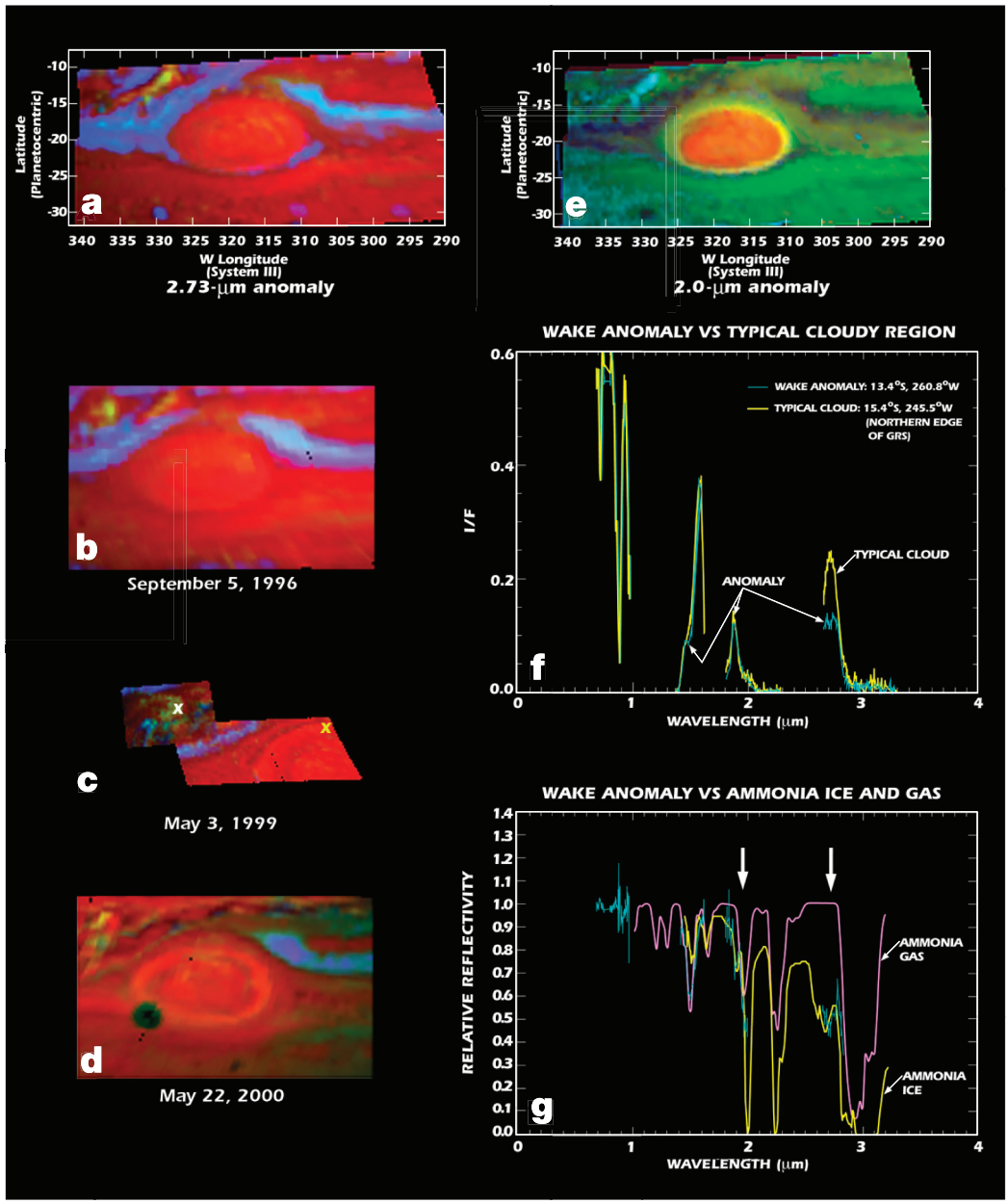

Plate 5, Figure 5.10: Representative images and spectra of the turbulent wake region northwest of the Great Red Spot, showing spectroscopically-identifiable ammonia clouds from Baines *et al.* (2002). Color renditions of *Galileo* NIMS images acquired during the first four years of Jupiter reconnaissance are shown in panels a–e. On the left (panels a–d), red denotes high reflectivity at 1.6 μm, indicative of optically thick clouds, blue denotes areas of high 5-μm flux transmitted through essentially clear atmospheric regions, and green denotes regions of low 2.73-μm reflectivity. The X symbols in panel c give locations of spectra plotted in panels f and g. The turbulent wake region is yellow, indicating a cloudy region of high 1.6-μm opacity and large 2.73-μm absorptivity indicative of ammonia ice absorption. In panel e (top right), this feature appears a pale color, indicative of a cloudy region of high 1.6-μm opacity (green) at high altitude (red, showing reflectivity in the highly absorbing 2.05-μm hydrogen feature) and low 1.99-μm absorption (blue, showing high 1.94-μm/1.99-μm band depth, indicative of strong ammonia absorption). The core of the Great Red Spot itself appears orange, indicative of its high altitude and high reflectivity. Surrounding it is a yellowish region showing a ring of material at slightly lower altitudes. A spectrum (blue curve in panel f) acquired of an anomalous feature on May 3, 1999 shows both the 1.99-μm and 2.73-μm absorptions compared to the high reflectivity seen in a nearby cloud of comparable altitude (yellow). The ratio of these two spectra is shown as the blue spectrum in panel g. This normalized spectrum effectively eliminates spectral artifacts due to overlying well-mixed gases such as hydrogen and methane. The resulting spectrum correlates well with ammonia ice (yellow) but not ammonia gas (pink), especially near 2.7 μm (right arrow) where ammonia gas does not absorb. Images acquired throughout the first four years of the *Galileo* reconnaissance (panels a–d) indicate that such spectroscopically-identifiable ammonia ice clouds occur frequently in the turbulent wake region northwest of the Great Red Spot.

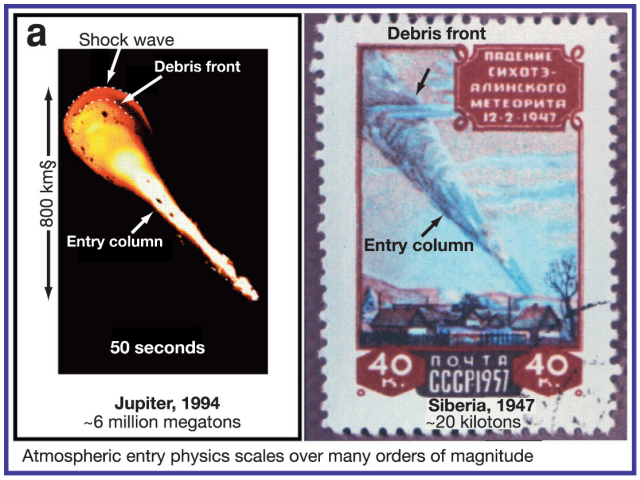

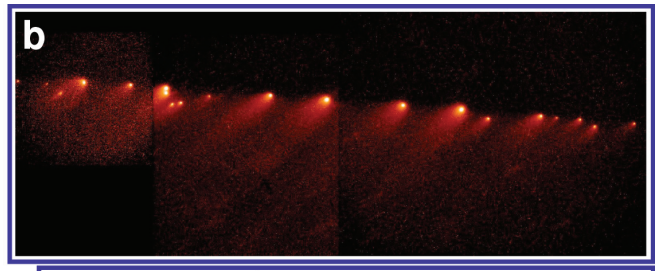

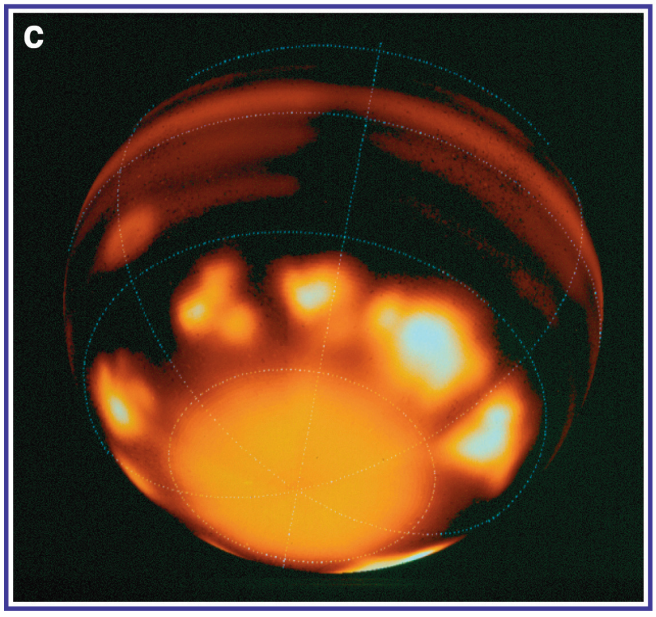

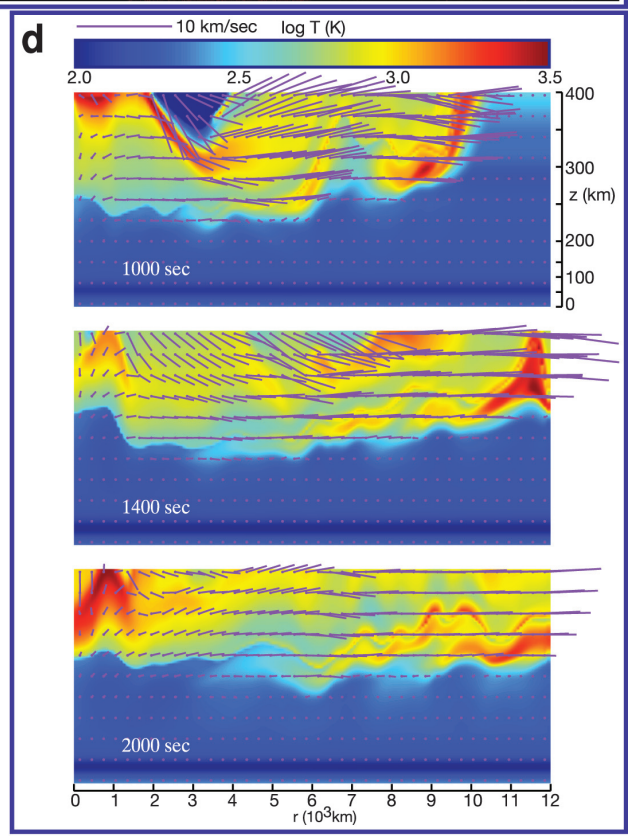

Plate 6, (a) Figure 8.1: Atmospheric impact physics over many orders of magnitude. Left: Model of SL9 plume by the Sandia group. Colors correspond to temperature. Note the extended entry/ejection column. Right: Eyewitness painting of 1947 Sikhote-Alin impact in Siberia by P. I. Medvedev. After Boslough Crawford (1997).

(b) Figure 8.2: Tops SL9 discovery image. Courtesy C. Shoemaker and D. Levy. Bottom: HST image of SL9 before impact. Courtesy H. Weaver and T. E. Smith (STScI) and NASA.

(c) Figure 8.3: Re-mapped composite of impact site images taken at 2.3 at the Palomar 5-meter telescope. In this strong CH_4 band, stratospheric aerosols deposited by the impacts stand out against the dark troposphere. Note also the high-altitude hazes above the south pole and the Great Red Spot.

(d) Figure 8.11: Atmospheric plume landing response model. Color is temperature, anchored streamers show flow. McGregor's ring shock is leaving the right edge of the grid, while the vanguard makes its final re-entry near the origin in the 1000 s panel. $z = 0$ is 1 bar pressure. Reprinted from Deming and Harrington (2001).

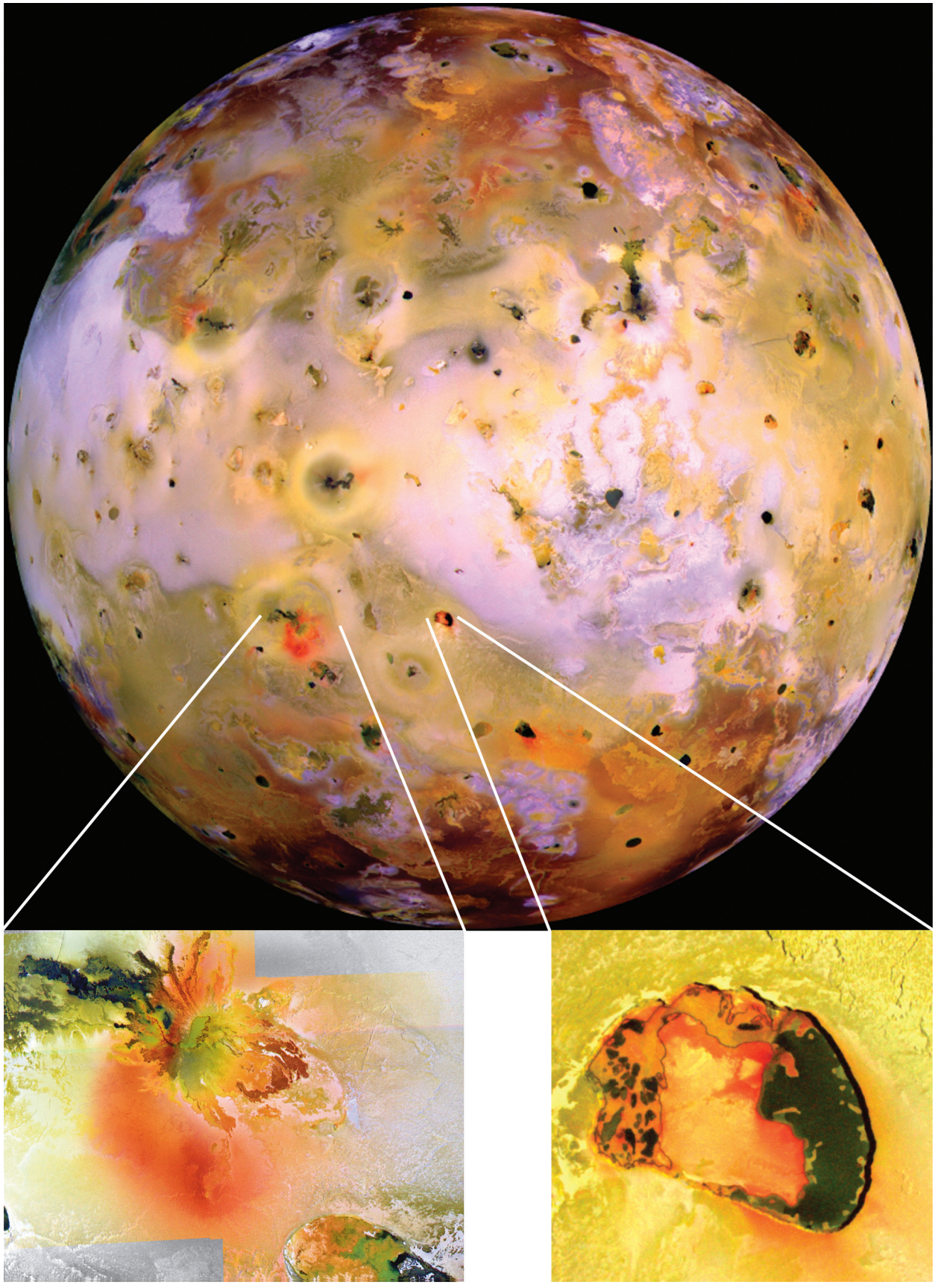

Plate 7, Figure 14.1: Full-disk color mosaic of Io's anti-jovian hemisphere acquired by *Galileo* in orbit C21, with insets showing high-resolution images of Tupan Patera from orbit C31 (lower right) and Culaan Patera from orbit I25 (lower left). All images are near true-color, but enhance the red colors because the 756 nm filter data was used in place of the red filter. Global image is 1.4 km/pixel, Culann was imaged at 200 m/pixel, and Tupan at 135 m/pixel. North is to the top in all images.

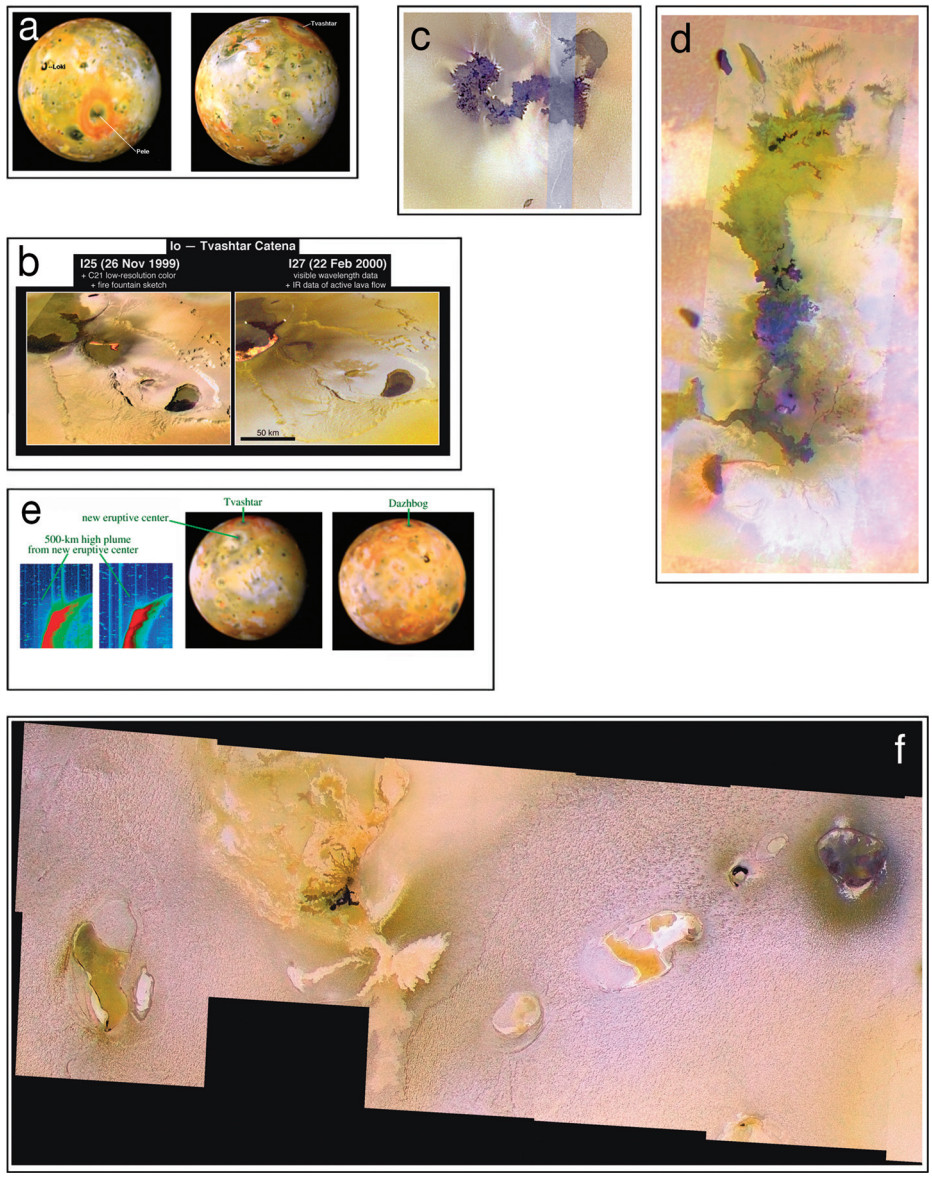

Plate 8, Figure 14.2: Collage of color images of Io. (a) Near-true color *Galileo* SSI images of Io from orbit G29 at a resolution of 10 km/pixel. Note the prominent red rings from the Pele and Tvashtar plumes. (b) Comparison of Tvashtar Catena as seen by *Galileo* SSI in orbits I25 and I27. I25 image has red lava drawn in as inferred from the position of bleeding pixels and colorized using C21 data. I27 image is true color except over the glowing lava which was made visible by overlaying data from SSI's three infrared filters on to the visible image. (c) *Galileo* SSI view of Prometheus Patera and surroundings from orbit I27. Mosaic is at 170 m/pixel and true-color with north to the top. (d) *Galileo* SSI near-true color view of the Amirani flow field from orbit I27. Center of image contains color data at 170 m/pixel, upper and lower parts of the flow field were imaged at 170 m/pixel only in the green filter, and the entire I27 data set was merged with the 1.4 km/pixel C21 global color data for context. (e) *Galileo* SSI views of tall high latitude plumes on Io from orbit I31. Pair of false-color eclipse images on the left are at 18 km/pixel and used the violet filter. Near-true color images on the right are at 19 km/pixel and use the violet, green, and 756 nm filters. (f) *Galileo* SSI view of the Chaac–Camaxtli region at 180–185 m/pixel from orbit I27. I27 data was collected in the clear filter then merged with the 1.4 km/pixel C21 global color data.

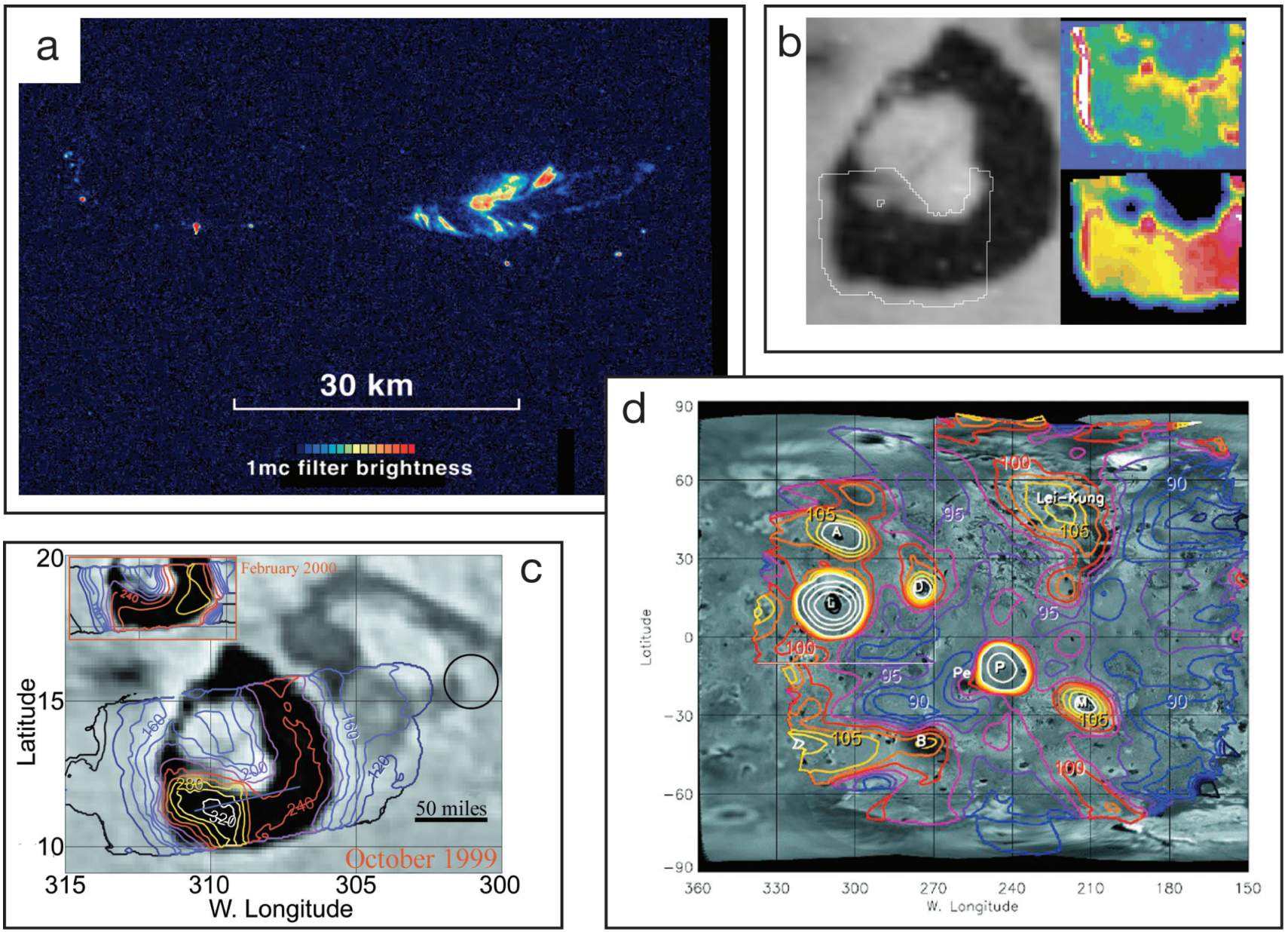

Plate 9, Figure 14.3: Collage of color images of Io. (a) *Galileo* SSI nighttime 1 m brightness image of Pele Patera from orbit I32. Image is at 60 m/pixel. (b) *Galileo* PPR nighttime temperature map of Loki Patera and surroundings from orbit I24. (c) *Galileo* NIMS nighttime brightness temperature maps of Loki Patera from orbit I32. Upper map is at 2.5 microns and lower map is at 4.4 microns. (d) PPR nighttime temperature map of a hemisphere of Io using data from orbits I25 and I27. A = Amaterasu, D = Daedalus, L = Loki, P = Pillan, Pe = Pele, M = Marduk, B = Babbar.

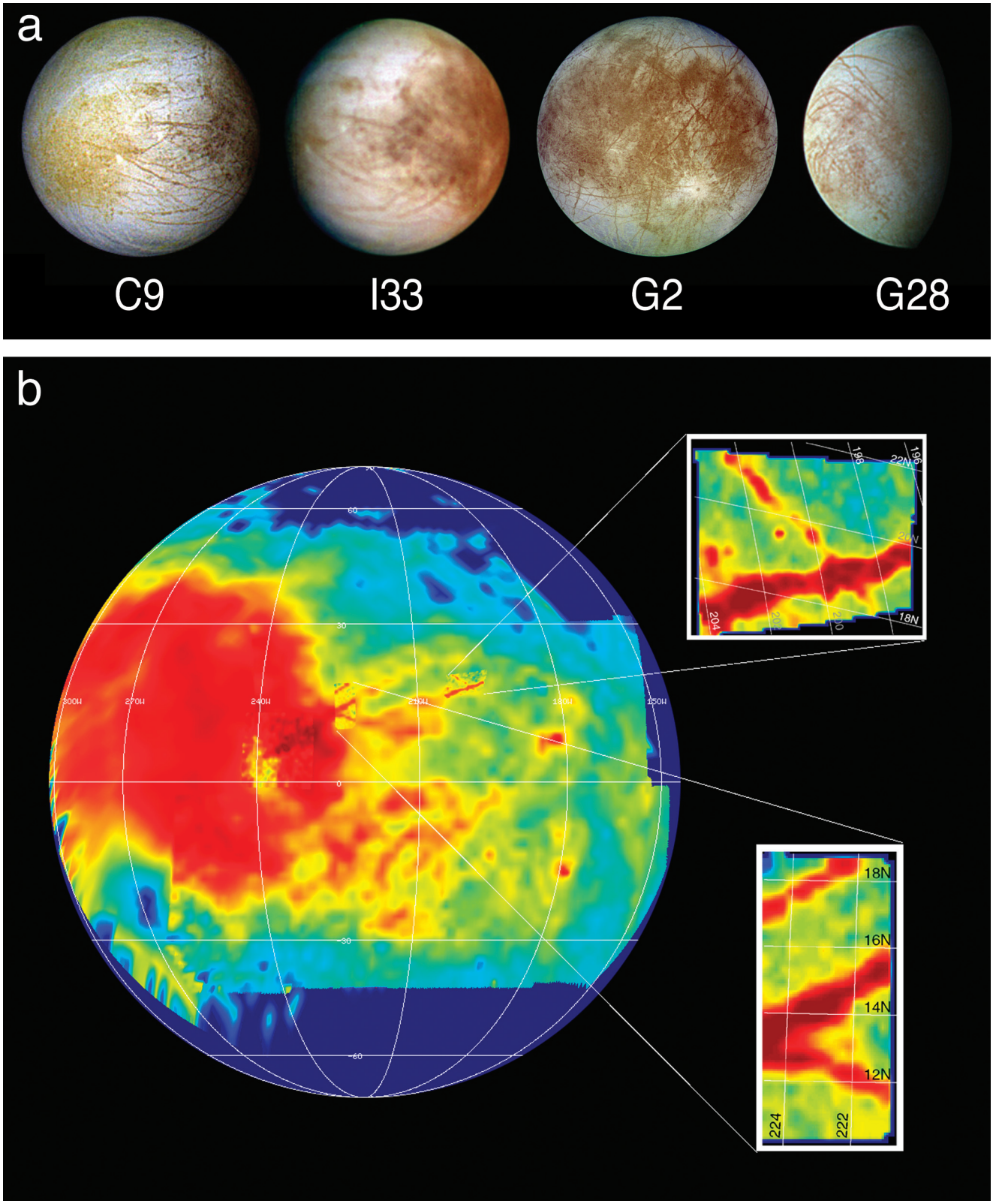

Plate 10, (a) Figure 15.1: These four false-color views of Europa were taken by the *Galileo* spacecraft to cover approximately the *leading hemisphere* (observation C9, centered at 0, 40° W), *subjovian hemisphere* (observation I33, centered 0, 9° W), *trailing hemisphere* (observation G2, centered at +1, 292° W), and *antijovian hemisphere* (G28, centered at −1, 147° W).

(b) Figure 15.4: Distribution of hydrated mineral spectral signature on Europa from the NIMS observations (from McCord *et al.* 1998b, 1999).

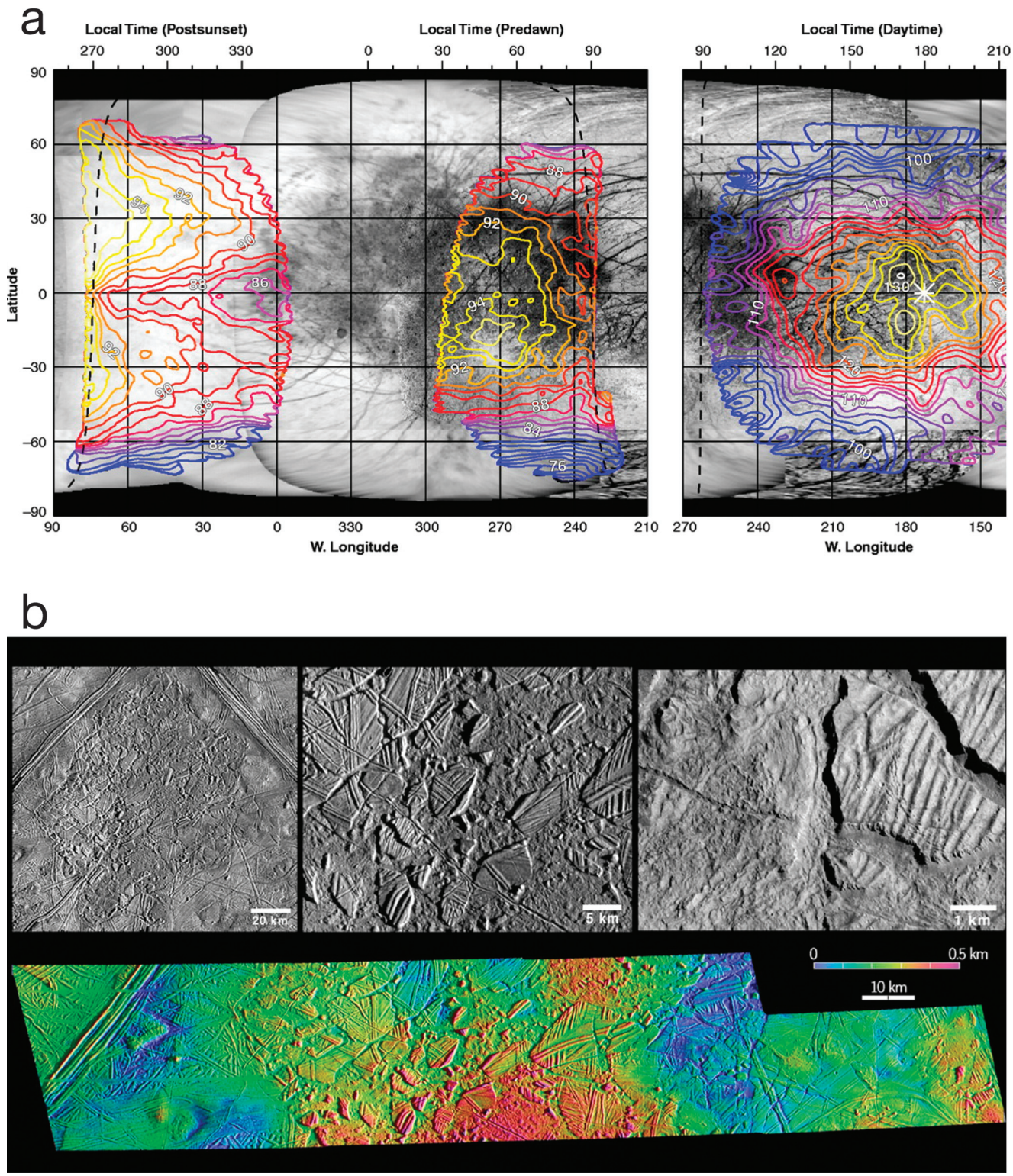

Plate 11, (a) Figure 15.2: Contours of brightness temperature distributions on Europa obtained from the *Galileo* Photopolarimeter-Radiometer (from Spencer *et al.* 1999).

(b) Figure 15.10: Conamara Chaos imaged at three scales, and corresponding topographic model: (left) regional-scale (180 m/pixel) view of Conamara shows its overall low albedo, angular boundaries, and location south of the intersection of two prominent ridges (E6ESDRKLIN01); (centre) at high resolution (54 m/pixel), it is apparent that polygonal blocks have translated and rotated in a mobile matrix (E6ESBRTPLN01); (right) at very high resolution (11 m/pixel), mass wasting is apparent along steep slopes, and craters and fractures in the matrix material indicate that it is brittle and immobile today (12ESCHAOS01); (bottom) topographic model across Conamara derived from stereo and photoclinometric techniques, showing that Conamara Chaos stands generally higher than its surroundings; color bar shows relative elevation (courtesy Paul Schenk).

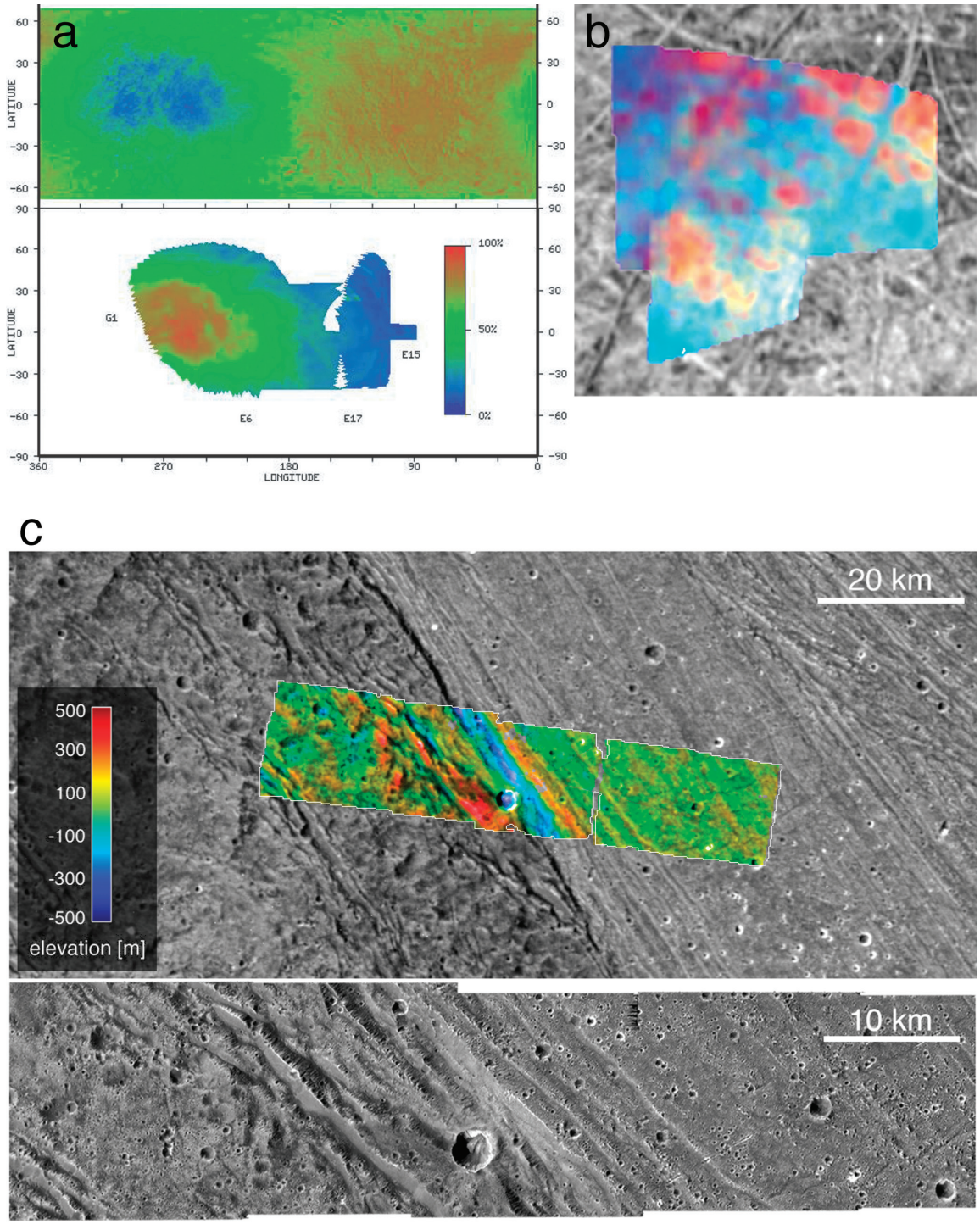

Plate 12, (a) Figure 20.2: Europa trailing hemisphere "bull's-eyes". (Top) *Voyager* ultraviolet (UV, 0.35 μm) to violet (VI, 0.41 μm) ratio map of Europa from McEwen (1986). Dark (blue) denotes more UV absorption relative to violet (VI). The trailing side enhancement was attributed to exogenic material such as sulfur implanted from the magnetosphere (McEwen 1986) or radiolytic processing producing sulfur (Johnson *et al.* 1988). (Bottom) Global distribution of Europa's hydrated material (Carlson *et al*. 2001, 2003b) obtained by the *Galileo* NIMS experiment. Because the abundance of this hydrate correlates with the ultraviolet absorption pattern shown in (a), they are suggestive of radiolytic processing of a hydrated sulfur compound as discussed in the text (e.g., Carlson *et al.* 1999b). Bull's-eye patterns are also found on Ganymede and Callisto (see text). Such patterns may be produced by asymmetries in the fluxes of both electrons and ions and corresponding radiolysis and implantation effects.

(b) Figure 20.10: Europa lineae and compositional variations. NIMS compositional map for approximately 182–188° W longitude, 4–10° N latitude overlayed on an SSI map. Hydrated material is shown as red, water ice is shown as blue. Note that the central bands of lineae are deficient in hydrated material compared to the margins. Diapiric heating can darken the margins by sublimating ice and leaving a sulfurous lag deposit.

(c) Figure 16.18: Margin between bright terrain of Harpagia Sulcus, and dark terrain of Nicholson Regio. (Top) Contextual view (121 m/pixel; 28BRTDRK02) with overlay of the stereo-based topographic data, and (bottom) high resolution (20 m/pixel; 28BRTDRK02) images show that the bright terrain of Harpagia is very smooth, with limited tectonic deformation. A progression of domino faults is inferred in dark terrain near the margin. Stereo data demonstrate that a deep bounding trough and an adjacent topographic high (inferred to be flexural in origin) occurs within the bright terrain (Giese *et al.* 2001, Nimmo *et al.* 2002). North is to the top of the context image.

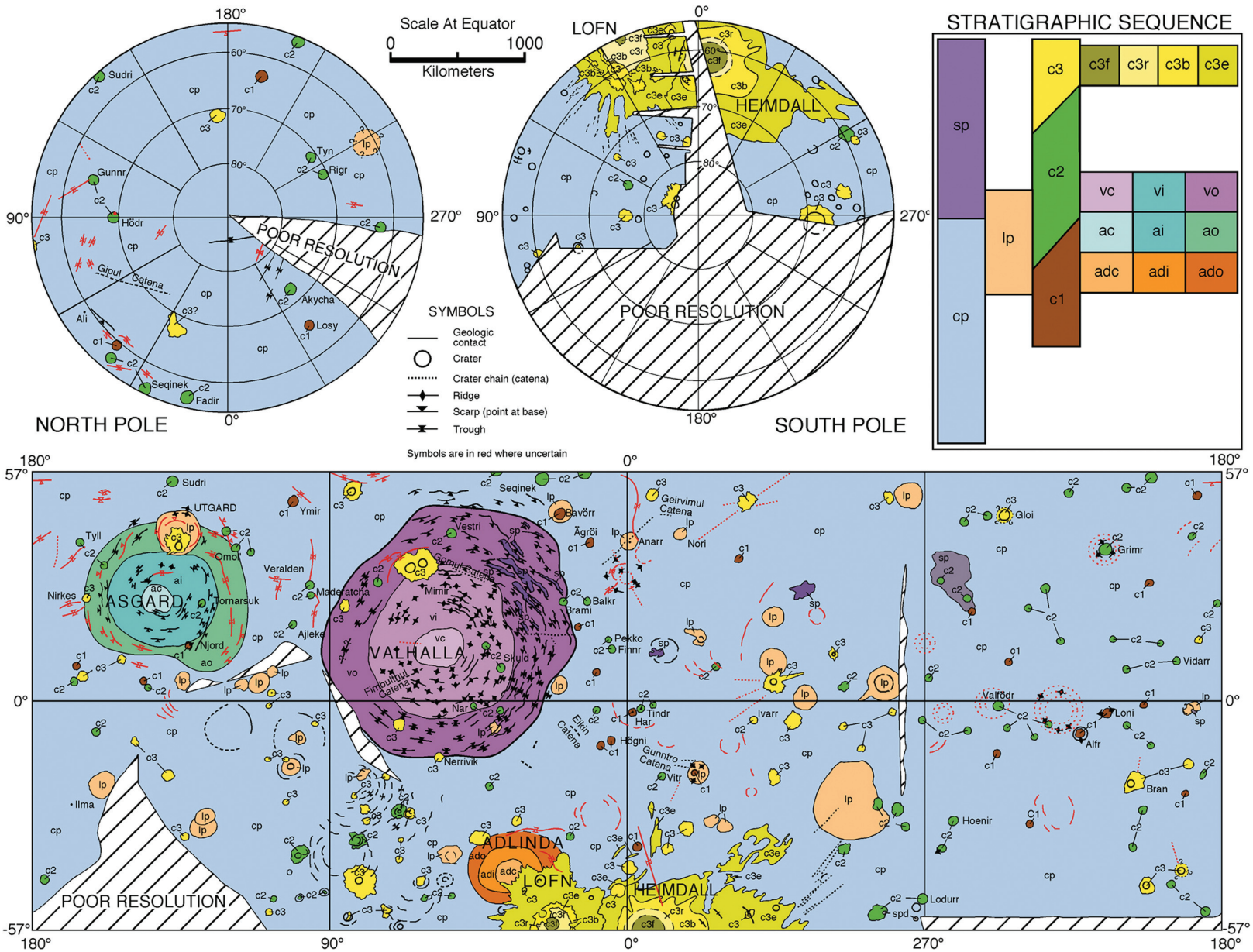

Plate 13, Figure 17.33: Geological sketch map of Callisto derived from that of Bender *et al*. (1997a) with additional mapping provided by *Galileo* imaging data; sp, lp, and cp refer to smooth plains, light plains, and cratered plains, respectively; c1, c2, and c3 refer to crater units, with c1 being oldest; c3 units are further subdivided into floor (f), rim (r), bright ejecta (b), and general ejecta (e) materials; units associated with Valhalla include central materials (vc), inner ring materials (vi) and outer ring materials (vo); Asgard multiring units include central materials (ac), inner ring materials (ai), and outer ring materials (ao); Adlinda multiring structure units include central materials (adi), and outer ring materials (ado). Greeley *et al*. (2000) subdivided crater deposits associated with Lofn and Heimdall into crater floor material (c3f), crater rim material (c3r), a bright ejecta facies (c3b), and general ejecta deposits (c3e). The distinction between the latter two units is that bright ejecta has a very high albedo, perhaps impact melt deposits rich in water ice, while the outer unit (c3e) may have been excavated from a shallower depth, hence containing more non-ice components, consistent with its lower albedo.

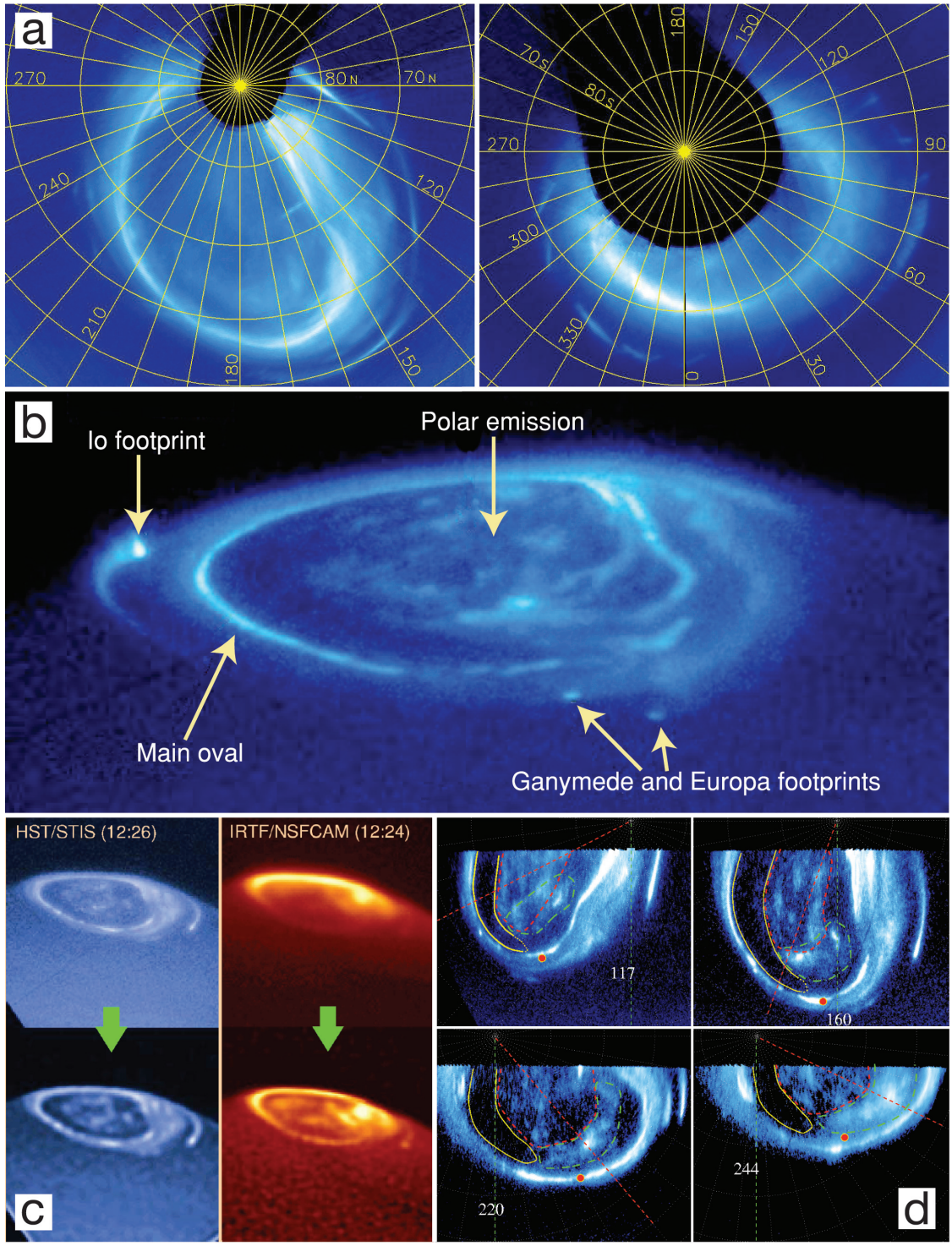

Plate 14, (a) Figure 26.10: Mean of all HST STIS images from Dec. 2000 – Jan. 2001 projected to views from above the north (upper) and south (lower) polar regions. Data are from Grodent *et al.* (2003a). Grid lines indicate System III longitude and planetocentric latitude lines. The arcs of emission at the lowest latitudes are from the Io footprint on different days.
(b) Figure 26.1: HST STIS UV image of Jupiter's northern aurora taken in Nov. 1998, showing the 3 different emission regions: the main oval, the satellite footprints, and the polar emissions. The image has been scaled with a logarithmic stretch in intensity to make clear the faint emissions next to brighter ones. Note the resolved auroral curtain above the limb, particularly in Io's magnetic footprint.
(c) Figure 26.6: Comparison of UV and H_3^+ IR images of Jupiter's aurora taken 2 min. apart on 16 Dec. 2000. The upper panels show the UV (left) and IR (right) images after standard reduction, before any additional processing. The lower panels show the same images after deconvolution and correction for limb brightening (IR – right) and blurring to the IR resolution followed by the same deconvolution (UV – left). The IR image has also been corrected for limb brightening. The differences in appearance of the IR and UV images are discussed in the text.
(d) Figure 26.16: Polar projections of Jupiter's aurora from STIS UV images on 16 Dec. 2000 (Grodent *et al.* 2003b). Polar emission regions outlined are the dark region (left, solid), the swirl region (central, dashed), and the active region (right, dot-dashed) at CML = 117, 160, 220, and 244°. The eastern end of the dark region appears dotted where it is not sharply defined. The latitude/longitude grid has a 10° spacing, the CML is marked with a vertical dashed line, and the $\lambda_{III} = 180°$ meridian is indicated with another dashed line. Dots indicate magnetic local noon mapped from 15 R_J using the VIP4 model.

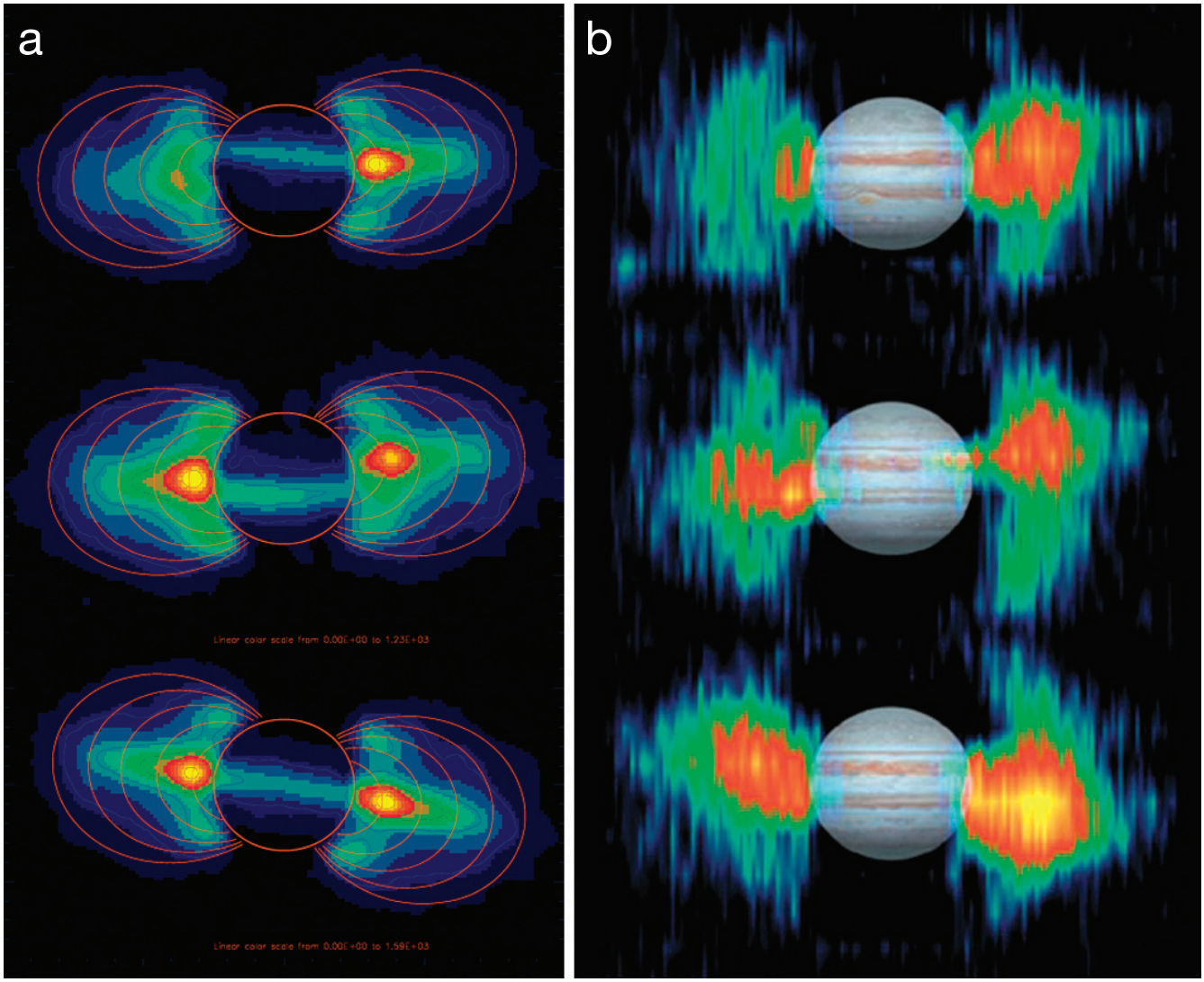

Plate 15, (a) Figure 27.11: VLA maps of Jupiter's synchrotron emission observed at 21 cm wavelength (1.4 GHz) in May 1997 when DE = 0°. Three orientations are shown corresponding to approximately 40, 180 and 280 degrees CML. The spatial resolution is approximately 0.25 R_J. Each image is averaged over approximately 40 degrees in longitude. The tilt of Jupiter magnetic equator and the two distinct emission regions (high latitude lobes and equatorial peaks) are clearly visible. Magnetic field lines corresponding to L = 1.5, 2.0, 2.5, 3.0 and 3.5 based on the VIP4 model are shown for reference. Note the high latitude lobe emission is associated with L 2.5 while the equatorial peak emission is closer to L 1.5. Thermal emission from the atmosphere has been subtracted. Courtesy of Bolton.
(b) Figure 27. 15 *Galileo* Color maps of Jupiter's synchrotron emission at 2.2 cm wavelength (13.8 GHz) obtained with the *Cassini* Radar instrument during the Jupiter flyby in 2001. Three orientations are shown corresponding to approximately 33, 177 and 285 degrees CML. The electrons responsible for synchrotron emission at 13.8 GHz are substantially higher energy than the electrons responsible for the emission at 1.4 GHz (see Figure 27.11). Map resolution is approximately 0.3 R_J. A visible image constructed from *Hubble Space Telescope* and *Voyager* data is shown superimposed for context. Thermal emission from the atmosphere has been subtracted. Courtesy of Bolton.

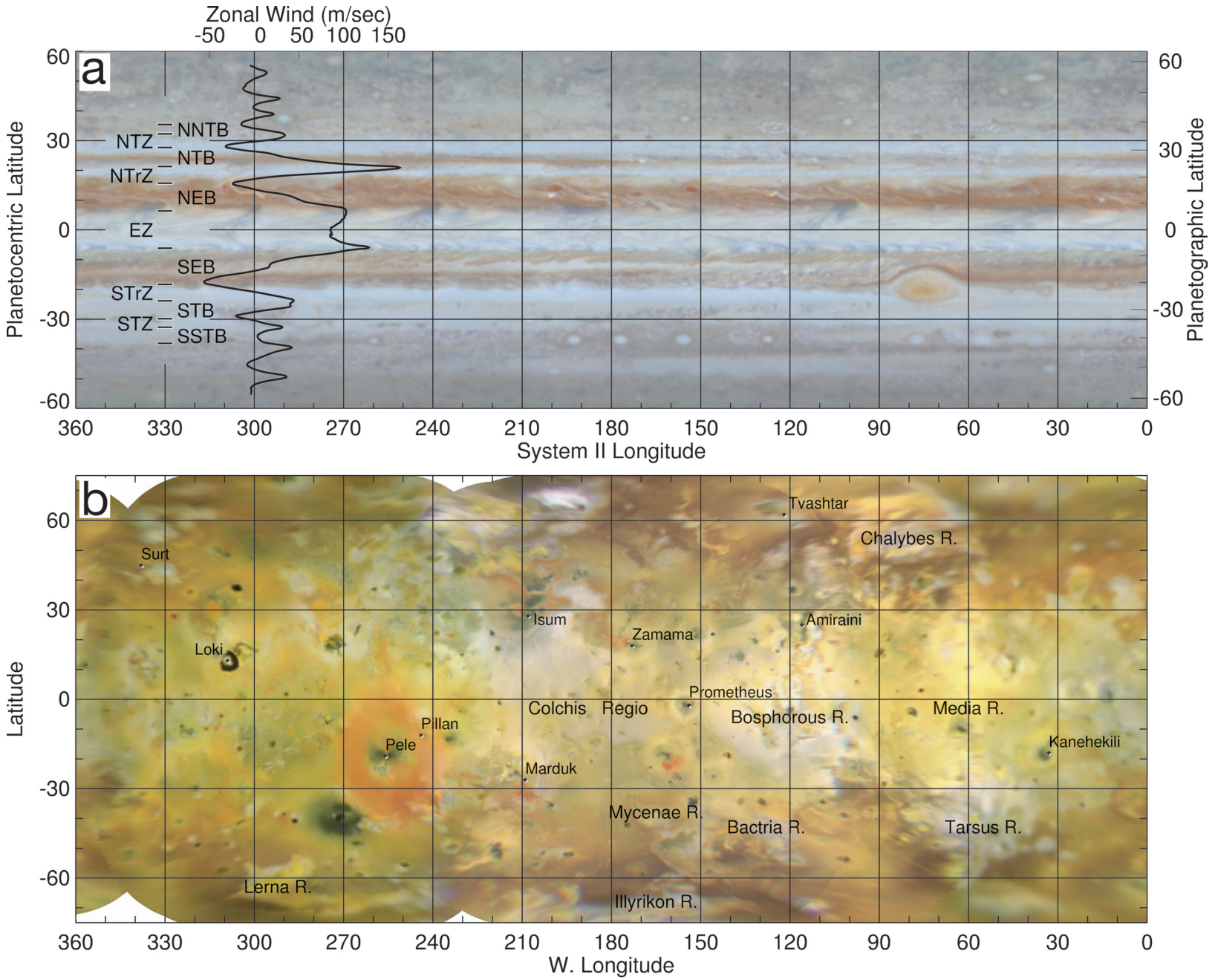

Plate 16 – A1.8 (a) Map of cloud bands of Jupiter with the zonal wind bands superimposed. (b) Map of Io.